

Characterization of the thermodynamic cycle of a MEMS-based external combustion resonant engine

H. Bardaweel · R. Richards · C. Richards ·
M. Anderson

Received: 6 October 2011 / Accepted: 16 March 2012 / Published online: 22 April 2012
© Springer-Verlag 2012

Abstract The thermodynamic cycle of a resonant, MEMS-based, micro heat engine is characterized. The micro heat engine is an external combustion engine made of a cavity encapsulated between two membranes. The cavity is filled with saturated liquid–vapor mixture working fluid. Heat is added to and rejected from the engine at a frequency corresponding to the resonant frequency of the engine. Both pressure–volume and temperature–entropy diagrams are used to investigate the thermodynamic cycle of the resonant micro heat engine. The results show that the working cycle is nearly rectangular in shape and consists of two constant temperature processes and two constant volume processes. We hypothesize that major sources of irreversibility in the engine are heat transfer over finite temperature differences during heat addition and rejection, heat transfer into and out of engine thermal mass, viscous losses due to liquid working fluid motion, and heat escape from the engine to the surroundings. The maximum pressure and volume changes measured inside the engine cavity are 45 Pa and 0.55 mm^3 , respectively. The results show that for a heat addition of 1 mJ, the engine operates over a very small temperature difference. The small operating temperature difference is mostly attributable to the large thermal storage of the engine structure, the membranes and the wicks. The measured second law efficiency of the micro heat engine is 16 %.

1 Introduction

Development of micro-scale engines based on standard macro-scale engines cycles has appealed to many research groups. Among these are micro-scale heat engines based on Rankine cycle (Frechette et al. 2003), Otto cycle (Fu et al. 2001), Brayton cycle (Isomura et al. 2006; Epstein et al. 1997; Mehra et al. 2000), Stirling cycle (Nakajima et al. 1989), and Humphrey cycle (Herrault et al. 2008). While macro-scale engines achieve both high power densities and high conversion efficiencies, the development of their micro-scale counterparts has proven challenging and daunting.

There are numerous obstacles that must be overcome to achieve a successful design and operation of the above-mentioned micro-scale engines (Frechette et al. 2003; Fu et al. 2001; Isomura et al. 2006; Epstein et al. 1997; Mehra et al. 2000; Nakajima et al. 1989; Herrault et al. 2008). Scaling down macro-scale engines to the micro-scale adds to the complexity of design and operation. As the dimensions of these engines shrink they become difficult to fabricate and operate (Herrault et al. 2008). That is, it is challenging to reproduce the complexity and three dimensionality of their macro-scale counterparts. Also, as the dimensions of these engines shrink, the operating frequency required to produce an appreciable amount of power increases, thus very high speeds may be required (Jacobson and Epstein 2003). This implies that some parts of the micro engine will be highly stressed, adding restrictions on the design process and material selection (Jacobson and Epstein 2003). Moreover, at the micro-scale level friction and viscous effects become dominant and limiting factors in rotating and translating systems (Jacobson and Epstein 2003). In addition, as the size of the engine shrinks it becomes harder to isolate the hot side of

H. Bardaweel · R. Richards · C. Richards (✉)
School of Mechanical and Materials Engineering,
Washington State University, P.O. Box 642920,
Pullman, WA 99164-2920, USA
e-mail: cill@wsu.edu

M. Anderson
Department of Mechanical Engineering,
University of Idaho, Moscow, ID 83844-0902, USA

the engine from the cold side, and thus the engine becomes thermally coupled. Finally, the problem of flame quenching remains an issue among the cycles employing internal combustion on the micro-scale.

The design of the MEMS-based resonant micro heat engine presented in this paper seeks to address many of the issues discussed above and to take advantage of unique possibilities offered by micro length scales. First, thermal power is conducted into the engine from an external heat source; thereby issues related to micro-scale combustion quenching are eliminated. The use of an external combustion heat engine also yields flexibility in the choice of a heat source, i.e. flames and waste heat are both candidates. Second, thermal power is converted to mechanical power through the expansion and compression of a two-phase working fluid by the oscillation of a flexible membrane. The use of a flexible membrane to expand and compress a two-phase working fluid eliminates the requirement to manufacture complex micromachines such as rotary compressors and turbines. Sliding contacts, such as found in reciprocating pistons and turbomachinery lead to relatively large frictional losses as the length scale is reduced (Jacobson and Epstein 2003). In contrast, flexing components, such as membranes or cantilevers do not suffer from sliding friction losses. Thus use of an expander that works by bending and flexing reduces frictional dissipation and simplifies engine manufacture.

The use of flexing components such as membranes or cantilevers permits the use of piezoelectric or electromagnetic transducers for conversion of the mechanical work produced by the expander to electrical work. Thus the generator can be directly coupled to and integrated with the engine structure, reducing complexity and cost. This impacts the operation of the engine as well. The use of flexing components with generating capacity (piezoelectrics or electromagnetics); i.e. electromechanical oscillators, means that operation of the engine at resonance is desirable.

The expansion of, heat addition to, compression of, and heat rejection from the working fluid all take place in a single cavity. In order for the cycle to take place in a single cavity the heat addition to and rejection from the engine must be intermittent. Thus this is an external combustion engine with periodic heat addition and rejection. This is distinct from a Rankine cycle for example, which because the working fluid circulates through the components, operates with steady heat addition. Therefore a switch is required to transport heat to and from the engine.

A benefit of decreasing engine size is that the magnitude of surface tension force increases as length scale becomes smaller. In conventional steam engines surface tension causes the liquid portion of a two-phase saturated mixture to form small droplets which can damage thermal machinery

during expansion and compression. However, if the engine can be scaled appropriately, surface tension can be used to hold the liquid portion of the two-phase saturated mixture to the walls of the cavity and thus prevent droplet formation. Since small droplets can be avoided, the compression and expansion of a two-phase saturated mixture becomes a practical option.

The implementation of these concepts results in the design shown schematically in Fig. 1. The engine consists of a single cavity which contains a saturated two-phase working fluid. The cavity is encapsulated between two thin membranes. The top membrane acts as an expander/compressor. The bottom membrane acts as an evaporator. A capillary wick fabricated on top of the evaporator membrane controls the thickness of the liquid-phase layer inside the cavity. A thermal switch is used to control the timing and duration of the heat addition and heat rejection processes. The working cycle the engine executes involves four processes as shown in Fig. 2. Heat is conducted into the engine from an external heat source and working fluid evaporates which causes the membrane to expand. Second, the membrane continues to flex out, expanding the two-phase working fluid. Third, heat is conducted out of the engine to an external heat sink and vapor-phase working fluid condenses which causes the membrane to flex in. Fourth, the membrane continues to flex back in, compressing the two-phase working fluid.

In previous work we have demonstrated operation of the engine and net power production at low operating frequencies, far from resonance (Cho et al. 2007a). Operation at resonance was shown to produce maximum work for a fixed amount of energy input to the engine (Bardaweel et al. 2008; Bardaweel et al. 2010). In the present work we focus on characterizing the thermodynamic cycle produced by the resonant engine. When the engine is operated at resonant frequency pressure and volume in the engine cavity are decoupled, i.e. they cyclically rise and fall approximately 90° out of phase, and cycle work is done. To accomplish this both vapor pressure and vapor volume

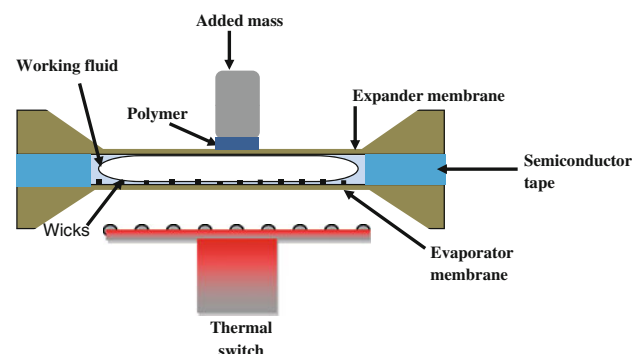


Fig. 1 Schematic of micro heat engine

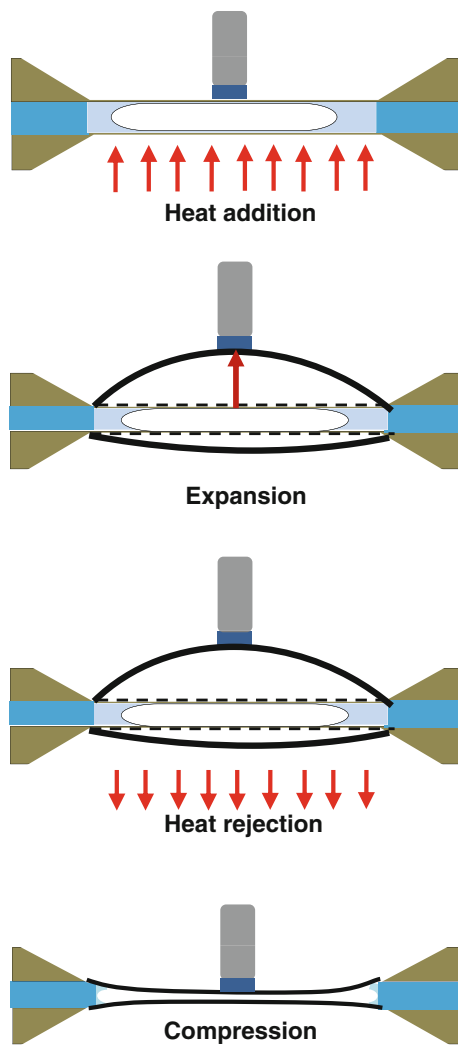


Fig. 2 Working cycle of resonant micro heat engine

inside the engine cavity are measured, from which both vapor temperature and vapor entropy inside the engine cavity can be deduced. Pressure–volume and temperature–entropy diagrams are then used to characterize the thermodynamic cycle of the resonant engine.

2 Experiment

2.1 Fabrication of resonant micro heat engine

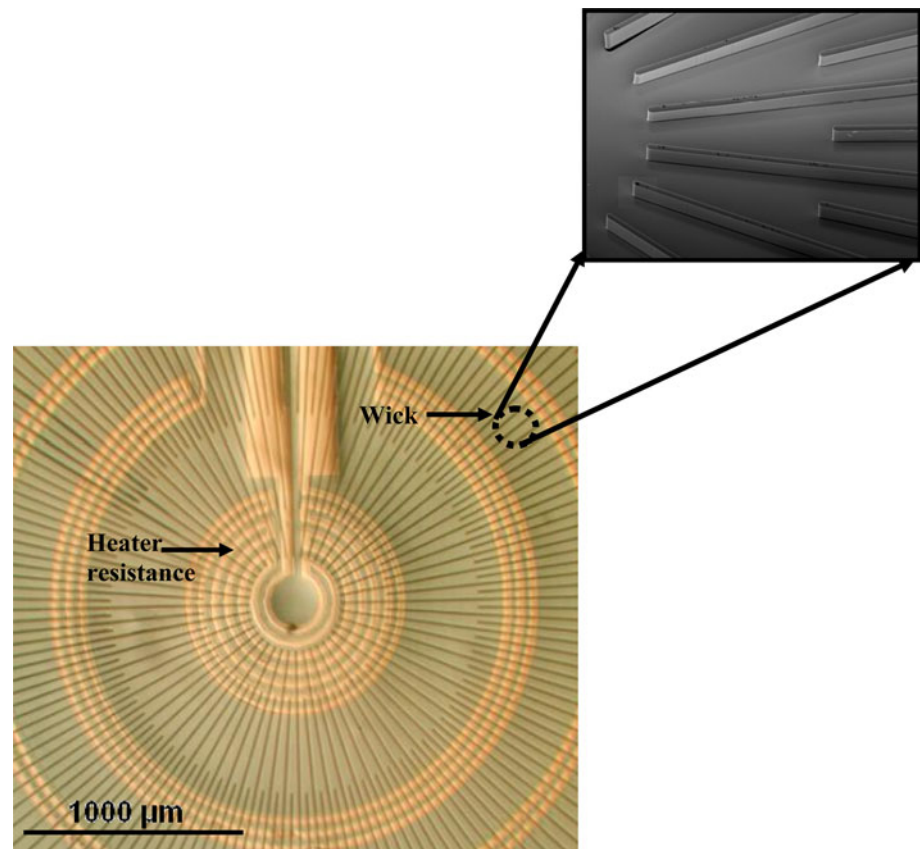
The major components of the micro heat engine; i.e., the expander, evaporator, and thermal switch are built using microfabrication technology. A brief description of the fabrication processes of the individual parts is documented in this article. Details on the fabrication of engine components are in (Bardaweel et al. 2008, 2010; Cho et al. 2006, 2007b).

Fabrication of the evaporator membrane starts with a 3 inch diameter double-sided polished silicon wafer. First, the wafer is placed in a furnace at 1,050 °C for 120 min to grow 500 nm thick oxide layers on both front and backside of the wafer. To prepare the wafer for boron diffusion, the backside of the wafer is masked, with a semiconductor tape, and the wafer is immersed in Buffered Oxide Etch (BOE) for 15 min. A boron diffusion process is then carried out, for 110 min at 1,125 °C in the furnace, to provide a 2.2 μm thick etch stop. Minor steps, including both BOE and low temperature oxide (LTO) processes, are, then, performed to remove the borosilicate glass layer formed as a result of boron diffusion. Next, a 5 nm adhesion layer of titanium/tungsten is sputtered on both sides of the wafer. Next, 300 and 500 nm gold layers are sputtered on front and back side of the wafer, respectively. A standard photolithographic process is then used to pattern the front side with resistance heaters. Likewise, the back side is patterned into 8 mm square window membranes. Next, wicks micro channel are fabricated on top of the resistance heater using an SU-8 polymer. The wicks take the shape of rectangular walls, radially patterned toward the center of the evaporator membrane. The wicks are 5 μm thick, 10 μm high, and spaced 90 μm apart. Potassium hydroxide anisotropic etching is then used to obtain the evaporator membranes. A fully fabricated evaporator membrane is shown in Fig. 3.

Fabrication of the expander membrane starts with a 3 inch diameter double-sided polished silicon wafer. A low pressure chemical vapor deposition (LPCVD) process is used to deposit a 300 nm thin layer of silicon nitride on both sides of the wafer. The back side of the wafer is then patterned into 10 mm square window membranes using a standard contact photolithographic process. Deep reactive ion etching (DRIE) followed by potassium hydroxide etching is then used to define the micro structure of the membranes.

The thermal switch controlling heat transfer to/from the micro engine takes the form of liquid–metal micro-droplets deposited in a square array on a silicon substrate. The array of liquid–metal (Hg) micro-droplets is fabricated by preferentially condensing mercury vapor onto gold targets patterned on a silicon die. First, the front side of a 3 inch diameter wafer is sputtered with a 5 nm adhesion layer of titanium/tungsten followed by a 300 nm layer of gold. The gold is then patterned via photolithography to produce a pattern of 30 μm diameter circular gold targets. Once the arrays of gold targets are fabricated, the wafer is diced and the rest of the fabrication process is carried out at the die level. Micro-droplet deposition occurs when the die is exposed to mercury vapor at 184 °C. As mercury preferentially condenses on the gold targets, micro-droplets form and grow on the gold targets.

Fig. 3 Fully fabricated evaporator membrane



2.2 Assembly of resonant micro heat engine

Assembly of the engine commences by fixing the evaporator membrane on a carrier plate. The cavity of the engine is then made by bonding layers of semi-conductor tape to the evaporator membrane die. The semiconductor tape is a flexible poly vinyl chloride (PVC) dicing tape, extensively used in micro-fabrication processes, characterized by high adhesion stability and high tear strength. Each layer is approximately 75 μm thick. The side length of the cavity is the same as the expander membrane side length, i.e., 10 mm. The thickness of the engine is controlled by varying the number of layers that make up the cavity walls. Next, a two-phase mixture of 3 M PF5060DL working fluid is injected into the cavity using a syringe. Carefully, the expander membrane is then clamped on top of the cavity. During this process a vapor bubble is formed in the center of the engine and a liquid annulus surrounds the bubble. An upper carrier is then screwed to the lower one and the plates are tightened to seal the cavity of the engine. A concentric mass is then placed on top of the expander membrane to reduce the resonant frequency of the engine to the order of 100 Hz (Bardaweel et al. 2010). To avoid shattering the expander membrane, and to reduce the thermal mass of the “added mass”, a low thermal conductivity polymer is used to separate the “added mass” from the engine, shown in Fig. 1. The “added mass”

is first bonded to the polymer and then placed on top of the engine.

2.3 Thermal switch-engine integration

To integrate the thermal switch with the micro engine the experimental apparatus shown in Fig. 4 is used. Upon assembly, the engine is mounted on top of an acrylic chamber. The chamber (ID = 4.0", OD = 4.5") is transparent to allow optical access and provide a seal to maintain a rough vacuum. Thermal switch is mounted inside the chamber facing the bottom of the engine, i.e., the evaporator membrane. The thermal switch is allowed to access the engine through a 10 × 10 mm hole in the acrylic chamber. A stainless steel shutter is used to open/close the hole between the thermal switch and the engine.

The thermal switch consists of a die with the liquid-metal micro-droplet array bonded to a micro heat exchanger. The array of patterned liquid-metal micro-droplets is used to make and break contact with the evaporator of the micro heat engine. When the micro-droplets make contact, and are squeezed between the two surfaces, the thermal switch is in its “on” state with increased heat transfer by conduction through the droplets (Cho et al. 2007b). When the micro-droplets break contact, leaving a gas gap between the two surfaces, the thermal switch is in its “off” state with reduced

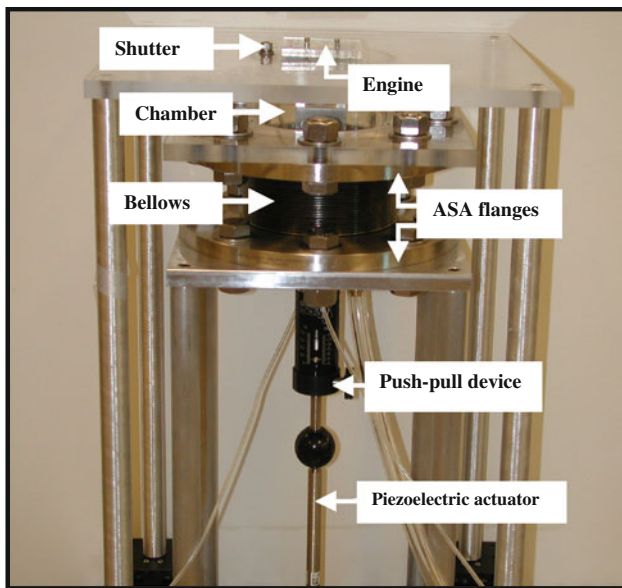


Fig. 4 Engine-thermal switch integration apparatus

heat transfer by conduction across the gas gap. It is important to note that the thermal switch is not activated by heat. It is a device, actuated by a piezoelectric, to control heat transfer by making and breaking thermal contact to quickly alternate between a low thermal resistance state and a high thermal resistance state.

During operation of the engine, air inside the chamber is replaced with argon gas. This is because argon has a relatively low thermal conductivity, compared to air, and so reduces heat leakage from the engine to the surroundings during the *off* state of the thermal switch (Cho et al. 2008). A piezoelectric actuator is used to actuate the thermal switch. A push–pull feed-through device is used to transmit the motion of the piezoelectric actuator, through the chamber, to the micro heat exchanger while maintaining an ultra-high vacuum seal. Because of the physical contact between the push–pull device and the chamber, vibration is transmitted to the engine. To eliminate the vibration transmission to the engine, edge welded metal bellows are used. The edge welded bellows are made of AMS-5512 alloy and have inner and outer diameters of 4.00" and 4.970", respectively. Two 9.00" ASA flanges are welded to the ends of the bellows to ensure the integrity of the vacuum seal.

While in previous work the micro heat engine was operated from a constant temperature, external heat source (Cho et al. 2007a), in the work documented in this article a resistance heater, patterned on top of the evaporator membrane, was used as the heat source. The use of resistance heater enabled precise control of the magnitude and duration of the heat addition process. The thermal switch was used to control heat rejection from the micro heat engine in the experiments.

2.4 Operation of resonant micro heat engine

Resonant operation of the micro heat engine is carried out using the setup shown in Fig. 5. To begin the experiment the chamber is isolated from the engine by closing the shutter. The air is pulled out of the chamber using a pump. Then argon is allowed to flow into the chamber until it reaches atmospheric pressure. Once the chamber is filled with argon the shutter is opened allowing the thermal switch access to the engine. A periodic voltage consisting of a unipolar square wave is applied across the resistance heater. Each time the voltage is applied electrical power is dissipated as heat and transferred into the evaporator membrane. Once heat is applied through the evaporator membrane, it evaporates the layer of liquid working fluid

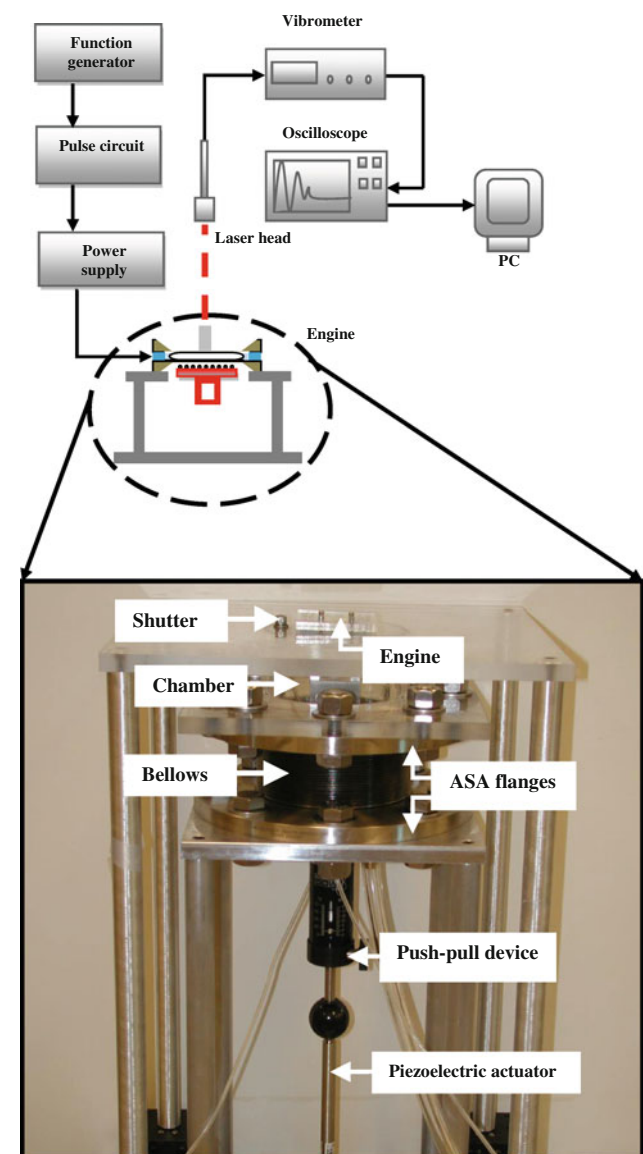


Fig. 5 Engine operation setup

held in the wicks. Likewise, when heat is removed from the engine, through the cold thermal switch, the vapor condenses. As heat is transferred into and then out of the working fluid, the quality and volume of the saturated mixture first increase and then decrease. Thus, periodic heat addition/removal from the evaporator membrane results in a periodic displacement of the expander membrane. The expander membrane acts like a piston in a conventional large-scale engine. However, instead of sliding in and out, the expander membrane flexes in and out. A laser vibrometer is used to monitor the displacements of the expander and evaporator membranes. Both displacements are sampled with a digital oscilloscope and stored on a personal computer for later analysis.

3 Analysis

To characterize the thermodynamic cycle of the micro heat engine at resonance, vapor pressure P , vapor volume V , vapor temperature T , and vapor entropy S inside engine cavity are determined. In the following analysis, it is assumed that working fluid inside engine cavity is saturated and that the pressure and temperature inside the cavity are uniform. Because pressure and volume during a resonant operation are decoupled, pressure and volume inside the cavity are measured independently (Bardaweel et al. 2010). Pressure inside the cavity P is obtained from the evaporator membrane deflection. Volume of the cavity V is detected from the deflection of the expander membrane. The volume underneath a membrane is determined by performing a double integral on the membrane deflection profile equation given by (Vlassak and Nix 1992).

$$V(\delta) = \frac{\delta}{a^4} \int_{-a}^a \int_{-a}^a (a^2 - x^2)(a^2 - y^2) \left[1 + \frac{R}{a^2}(x^2 + y^2) \right] dx dy \quad (1)$$

where δ is the deflection midpoint of the expander membrane in micrometer, a is $\frac{1}{2}$ the side length of the membrane, x and y are coordinates on the membrane, and $R = 0.34$ is a constant determined by matching the deflection profile of the equation to experimental data. For a 10 mm expander square membrane used in this work, the integral (1) simplifies to

$$V(\delta) = \delta \frac{16}{45} a^2 (2R + 5). \quad (2)$$

Pressure P is related to the deflection of the evaporator membrane through a calibrated pressure deflection curve of the form (Vlassak and Nix 1992)

$$P = C_1 \delta + C_2 \delta^3, \quad (3)$$

where pressure P is in kPa, δ is the evaporator membrane deflection in micrometer. The constants C_1 and C_2 are determined by matching the deflection profile of the equation to experimental data. For the 2.2 μm thick, 64 mm² silicon evaporator membrane used in this work the constants C_1 and C_2 are $1.42 \times 10^{-2} \text{ kPa} \cdot \mu^{-1}$ and $8.4 \times 10^{-6} \text{ kPa} \cdot \mu^{-3}$, respectively.

Based on pressure P and volume V measurements, the boundary work of the engine is defined as

$$W = \int P dV. \quad (4)$$

The thermal efficiency is defined based on the boundary work W in (4) and the input energy delivered to the engine per cycle E , given by

$$\eta_{th} = \frac{\int P dV}{E}. \quad (5)$$

The Carnot efficiency is defined based on the maximum and minimum temperatures of the working fluid and given by

$$\eta_{Carnot} = 1 - \frac{T_{Li}}{T_{Hi}} \quad (6)$$

where T_{Li} and T_{Hi} are the minimum and maximum engine cavity temperatures, respectively. Using pressure measurements P , temperature inside the cavity T is interpolated from thermodynamic tables of PF5060 working fluid.

To obtain the temperature-entropy diagram entropy S of engine cavity is sought. However, entropy S may not be specified from direct measurements. To specify the entropy S , two independent intensive properties are needed (Cengel and Boles 1994). Entropy S is obtained using quality and pressure information. The quality of the mixture \bar{Q} along with pressure P serve as the two intensive properties needed. The quality of the mixture \bar{Q} is calculated based on volume V and density ρ :

$$\bar{Q} = \frac{V \times \rho}{m_{total}} \quad (7)$$

The product $(V \times \rho)$ represents the mass of vapor inside the cavity. The total mass of liquid–vapor mixture is given by m_{total} . The vapor density ρ is interpolated using thermodynamic tables of PF5060 working fluid. Entropy S is then given by

$$S = \bar{Q} \cdot S_{fg}, \quad (8)$$

$$S_{fg} = S_g - S_f, \quad (9)$$

where S_g and S_f are entropies of saturated vapor and saturated liquid, respectively.

4 Results and discussion

To operate the engine at resonance first the resonant frequency of the engine is measured. Table 1 lists the properties of the micro heat engine used in this work. The resonant frequency f_n of the engine is determined using a “tuning fork” ring-down technique. That is, the engine is operated by applying periodic heat pulses with fundamental frequencies of $f_o = 0.1, 1$ and 10.0 Hz. The operation of the engine at these frequencies allows it to oscillate to the static position. The expander membrane deflection takes the form of a decaying sinusoid (ring-down). This ring-down response is measured with the laser vibrometer and then analyzed by taking a Fourier transform of the measured ringing. Resonant frequency is then determined from the frequency spectrum of the ring-down data (Bardaweel et al. 2008, 2010). That is, the resonant frequency of the engine is determined by determining the frequency at which the peak in deflection amplitude is observed. Figure 6 shows frequency response of the expander membrane deflection (ring-down). The resonant frequency f_n of this particular engine is determined to be $f_n = 115$ Hz.

The thermodynamic cycle of the micro heat engine is examined next. In the experiment, the micro heat engine is operated at its resonant frequency, $f_n = 115$ Hz. Since the focus of this work is characterization of the thermodynamic cycle rather than maximizing work output, a very small amount of heat is delivered to the engine each cycle. This ensures that there is no shift in resonant frequency due to transient heating effects. Input energy per cycle, delivered to the evaporator, is $E = 1.0$ mJ and it is delivered with a 1 % duty cycle. The thermal switch, controlling heat rejection, is maintained at 4°C during the operation of the engine. The experiment is carried out at room temperature, $T_o = 294$ K. The saturation pressure of the two-phase mixture inside the engine cavity is $P_{sat} = 25,351$ Pa gauge at room temperature $T_o = 294$ K.

Figure 7 shows the time history of pressure and volume inside the cavity when the engine is operated at resonance, $f_n = 115$ Hz. Volume and pressure inside engine cavity are obtained from (2) and (3), respectively. Figure 7 reveals that the pressure and the volume in the engine cavity are

Table 1 Resonant micro heat engine specifications

Expander side length (mm)	10
Expander thickness (nm)	300
Evaporator side length (mm)	8
Evaporator thickness (μm)	2.2
Cavity thickness (μm)	150
Bubble size (mm)	9.0
Added mass (gram)	3.9

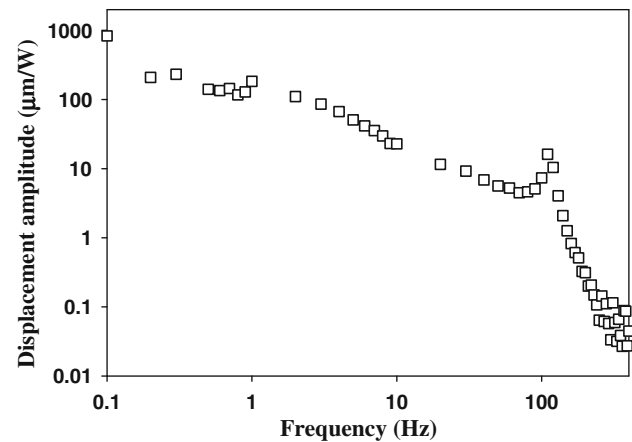


Fig. 6 Frequency response of expander membrane deflection

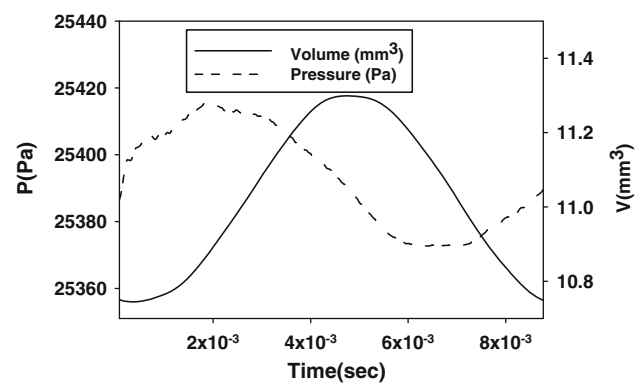


Fig. 7 Pressure and volume—time history at resonance, $f_n = 115$ Hz

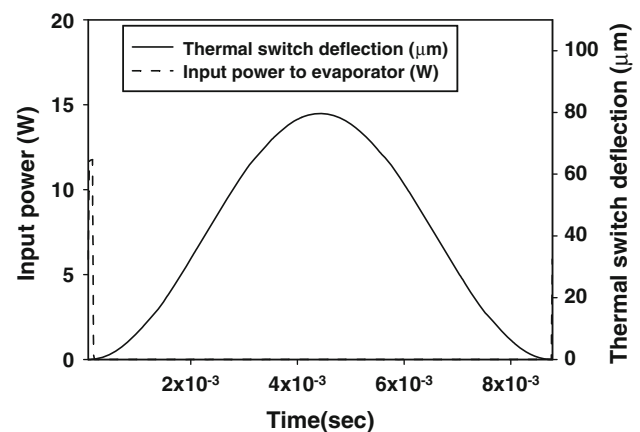


Fig. 8 Power input to the engine and deflection of the thermal switch—time history

decoupled, or out of phase by approximately 90° . Also, shown in Fig. 8 is time history of both power input to the engine and displacement of the thermal switch. In Fig. 8 the input power, in Watts, delivered to the evaporator membrane (through the resistance heater) is plotted on the

left vertical axis. The displacement of the thermal switch is plotted on the right vertical axis. As the thermal switch moves from its initial position (0 μm) to its final position (80 μm) it closes the gap between the liquid–metal micro-droplet array and evaporator membrane and thus heat rejection takes place. As a result, heat is conducted away from the engine (higher temperature) to the thermal switch (lower temperature).

Pressure–volume and temperature–entropy diagrams are shown in Figs. 9 and 10, respectively. The cycle work is represented by the area enclosed by the pressure–volume and temperature–entropy diagrams. The maximum pressure rise and volume change inside the cavity are 45 Pa and 0.55 mm^3 , respectively. The engine is operating over a very small temperature difference, on the order of 1 K. At this condition the mechanical work produced by the micro engine in one cycle is 0.018 μJ . The small operating temperature difference is due partly to the small amount of heat added and to the large thermal storage of the engine structure, the membranes and the wicks. That is, very little

of the heat that is added to the engine goes to vaporizing working fluid, <10 %.

To calculate the Carnot efficiency (Eq. 6), the engine may be viewed as operating between the two temperature reservoirs at T_{Hi} and T_{Li} , respectively. The second law efficiency, the ratio of the thermal efficiency to the Carnot efficiency is then found to be 16 %. The thermal efficiency is evaluated from the ratio of the work produced by the working fluid to the energy added to the membrane (Eq. 5).

From the pressure–volume and temperature–entropy diagrams it can be seen that the cycle is roughly rectangular in shape and consists of two constant temperature processes and two constant volume processes. Heat is transferred from the engine structure to vaporize the working fluid in a constant temperature process. During this process the membrane is moving outward and vapor volume increases. After vaporization is completed, due to inertial effects, the membrane continues to move outwards for a short time and the temperature and pressure drop slightly. Once the expander membrane reaches its maximum deflection point, the thermal switch closes the gap with the evaporator membrane and heat is conducted away from the engine structure. Engine pressure and temperature decrease over a very small volume change. During resonant operation of the engine, potential energy is stored in the flexing expander membrane. This energy stored in the expander membrane now causes the membrane to flex in reducing the volume. During this process heat is removed from the vapor and condensation occurs at constant temperature. Again, due to inertial effects, the expander membrane continues to move down after condensation has ceased. When the membrane reaches its minimum deflection point, heat is added to the engine structure through the evaporator membrane. The inertial effects are relatively small in these experiments due to the small deflections resulting from small heat addition. With resonant operation at higher amplitudes, the inertial effects would become more dominant producing distinctive compression and expansion processes.

Engine irreversibility may be attributed to three major sources: (1) entropy production due to the finite temperature differences required to drive heat transfer during heat addition and rejection (2) entropy production due to heat transfer into and out of thermal storage in the engine, and (3) entropy production due to viscous losses in the liquid working fluid surrounding the vapor bubble. The first mechanism, entropy production due to heat transfer into and out of the engine, is a consequence of the fact that the engine is an external combustion device. The second mechanism, entropy production due to heat transfer into and out of thermal storage is a consequence of the resonant operation of the engine with its periodic heat addition and rejection processes. Finally, the third mechanism, entropy

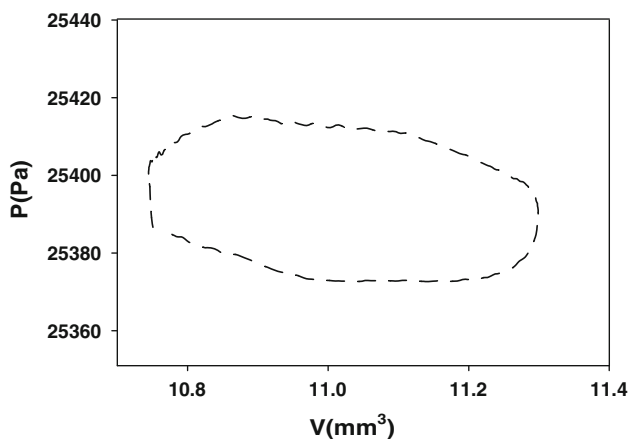


Fig. 9 Pressure-volume diagram at resonance, $f_n = 115$ Hz

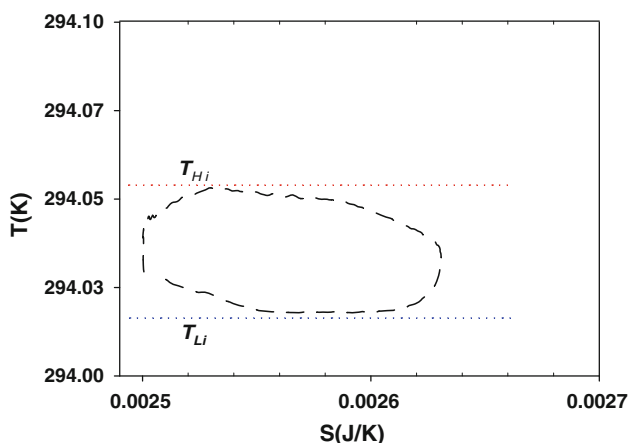


Fig. 10 Temperature-entropy diagram at resonance, $f_n = 115$ Hz

production due to viscous losses is a consequence of the motion of the liquid working fluid as the membrane flexes in and out. Thus, heat transfer between engine components and external heat source/sinks contribute to the external irreversibility of the engine, while viscous effects contribute to the internal irreversibility of the engine. Both external irreversibility and internal irreversibility lower the performance of the engine and cause loss in the available work.

5 Conclusions

The cycle of the resonant MEMS-based micro heat engine has been acquired experimentally. The thermodynamic cycle of the resonant micro heat engine has been characterized using both pressure–volume and temperature–entropy diagrams. The working cycle is nearly rectangular in shape and consists of two constant temperature processes and two constant volume processes. Major sources of irreversibility in the engine are believed to be heat transfer over finite temperature differences during heat addition and rejection, heat transfer into and out of engine thermal mass, viscous losses due to liquid working fluid motion, and heat escape from the engine structure to the surrounding. The maximum pressure and volume changes measured inside engine cavity are 45 Pa and 0.55 mm³, respectively. The results show that for a heat addition of 1 mJ, the engine operates over a very small temperature difference. The small operating temperature difference is mostly attributable to the large thermal storage of the engine structure, the membranes and the wicks. The measured second law efficiency of the micro heat engine is 16 %.

References

- Bardaweel HK, Anderson MJ, Richards RF, Richards CD (2008) Optimization of the dynamic and thermal performance of a resonant micro heat engine. *J Micromech Microeng* 18:104014. doi:[10.1088/0960-1317/18/10/104014](https://doi.org/10.1088/0960-1317/18/10/104014)
- Bardaweel H, Anderson M, Richards R, Richards C (2010) Cyclic operation of a MEMS-based resonant micro heat engine: experiment and model. *J Appl Phys* 107:104901. doi:[10.1063/1.3372755](https://doi.org/10.1063/1.3372755)
- Cengel Y, Boles M (1994) Thermodynamics an engineering approach. McGraw Hill, New York
- Cho J, Richards C, Jiao J, Bahr R, Richards R (2006) Design and characterization of a MEMS thermal switch. In: Proceedings of the solid-state sensors, actuators, and microsystems workshop
- Cho JH, Weiss LW, Richards CD, Bahr DF, Richards RF (2007a) Power production by a dynamic micro heat engine with an integrated thermal switch. *J Micromech Microeng* 17:S217–S223. doi:[10.1088/0960-1317/17/9/S02](https://doi.org/10.1088/0960-1317/17/9/S02)
- Cho J, Wiser T, Richards C, Bahr D, Richards R (2007b) Fabrication and characterization of thermal switch. *Sens Actuators A* 133:55–63. doi:[10.1016/j.sna.2006.03.033](https://doi.org/10.1016/j.sna.2006.03.033)
- Cho JH, Richards CD, Richards RF (2008) A facility for characterizing the steady-state and dynamic thermal performance of microelectromechanical system thermal switches. *Rev Sci Instrum* 79:034901. doi:[10.1063/1.2894147](https://doi.org/10.1063/1.2894147)
- Epstein AH et al (1997) Micro-heat engines, gas turbines and rocket engines: the MIT micro engine project. In: Proceedings of the 28th AIAA fluid dynamics conference
- Frechette L, Lee C, Arslan S, Liu Y-C (2003) Design of a microfabricated Rankine cycle steam turbine for power generation. In: Proceedings of the ASME IMECE 2003: IMECE2003-42082
- Fu K, Knobloch AJ, Martinez FC, Walther DC, Fernandez-Pello C, Pisano AP, Liepmann D (2001) Design and fabrication of a silicon based MEMS rotary engine. In: Proceedings of the ASME IMECE 2001: MEMS-23925
- Herrault F, Crittenden T, Yorish S, Birdsall E, Glezer A, Allen MG (2008) A self-resonant, MEMS-fabricated, air-breathing engine. In: Proceedings of the solid-state sensors, actuators, and microsystems workshop, Hilton Head Island, South Carolina
- Isomura K, Murayama M, Teramoto S, Hikichi K, Endo Y, Togo S, Tanaka S (2006) Experimental verification of the feasibility of a 100 W class micro-scale gas turbine at impeller diameter of 10 mm. *J Micromech Microeng* 16:S254–S261. doi:[10.1088/0960-1317/16/9/S13](https://doi.org/10.1088/0960-1317/16/9/S13)
- Jacobson SA, Epstein AH (2003) An informal survey of Power MEMS. In: Proceedings of the ISMME2003-K18, Tsuchiura, Japan
- Mehra A, Zhang X, Ayon AA, Waitz IA, Schmidt MA, Spadaccini CM (2000) A six-wafer combustion system for a silicon micro gas turbine engine. *J Microelectromech Syst* 9:517–527
- Nakajima N, Ogawa K, Fujimasa I (1989) Study on micro engines—miniaturizing stirling engines for actuators and heat pumps. In: Proceedings of the IEEE Micro electro mechanical system workshop
- Vlassak J, Nix W (1992) A new bulge test technique for the determination of young's modulus and Poisson's ratio of thin films. *J Mater Res* 7:3242–3249. doi:[10.1557/JMR.1992.3242](https://doi.org/10.1557/JMR.1992.3242)